

Coaxial Si/anodic titanium oxide/Si nanotube arrays for lithium-ion battery anodes

Jiepeng Rong^{1,§}, Xin Fang^{1,§}, Mingyuan Ge¹, Haitian Chen², Jing Xu¹, and Chongwu Zhou² (✉)

¹ Mork Family Department of Chemical Engineering and Materials Science, University of Southern California, Los Angeles, California 90089, USA

² Ming Hsieh Department of Electrical Engineering, University of Southern California, Los Angeles, California 90089, USA

[§] These authors contributed equally to this paper.

Received: 20 June 2012

Revised: 9 January 2013

Accepted: 10 January 2013

© Tsinghua University Press
and Springer-Verlag Berlin
Heidelberg 2013

KEYWORDS

lithium ion battery,
anodic titanium oxide,
silicon anode

ABSTRACT

Silicon (Si) has the highest known theoretical specific capacity (3,590 mAh/g for $\text{Li}_{15}\text{Si}_4$, and 4,200 mAh/g for $\text{Li}_{22}\text{Si}_4$) as a lithium-ion battery anode, and has attracted extensive interest in the past few years. However, its application is limited by poor cyclability and early capacity fading due to significant volume changes during lithiation and delithiation processes. In this work, we report a coaxial silicon/anodic titanium oxide/silicon (Si-ATO-Si) nanotube array structure grown on a titanium substrate demonstrating excellent electrochemical cyclability. The ATO nanotube scaffold used for Si deposition has many desirable features, such as a rough surface for enhanced Si adhesion, and direct contact with the Ti substrate working as current collector. More importantly, our ATO scaffold provides a rather unique advantage in that Si can be loaded on both the inner and outer surfaces, and an inner pore can be retained to provide room for Si volume expansion. This coaxial structure shows a capacity above 1,500 mAh/g after 100 cycles, with less than 0.05% decay per cycle. Simulations show that this improved performance can be attributed to the lower stress induced on Si layers upon lithiation/delithiation compared with some other recently reported Si-based nanostructures.

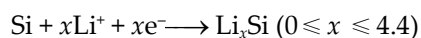
1 Introduction

Increasing efforts have been devoted to the development of lithium-ion batteries with higher energy density, higher charging and discharging rates, and longer cycle life, to meet the requirement of the

ever growing portable electronic and next-generation electrical vehicles industry [1–13]. Silicon has drawn particular attention as an anode material for lithium-ion batteries primarily because it has the highest known theoretical capacity (3,590 mAh/g for $\text{Li}_{15}\text{Si}_4$, and 4,200 mAh/g for $\text{Li}_{22}\text{Si}_4$), which is nine times higher

Address correspondence to chongwuz@usc.edu

than that of commercial graphite anodes and other oxide and nitride materials [14]. However, its application is restricted by severe capacity fading caused by pulverization, which is due to large volume expansion and contraction during the lithiation and delithiation processes



Thus far, it has been evidenced that nanostructured Si can be utilized to obtain improved electrochemical performance over bulk Si and promising candidates for high performance lithium-ion battery anodes include Si nanowires (NWs) [15–17], carbon–Si core–shell NWs [18], carbon–Si nanocomposites [19, 20], TiSi_2/Si

nanonets [21], three-dimensional porous Si [22, 23], and sealed Si nanotubes [24]. These studies indicate that the key feature for electrode design is providing enough free space around Si so that large volume expansion can be accommodated. In addition, Si nanostructures grown directly on a metallic current collector should enhance both power density and energy density of lithium-ion batteries by minimizing internal resistance and the usage of non-active materials, such as carbon black and binder.

Here we report a coaxial silicon/anodic titanium oxide/silicon (Si–ATO–Si) nanotube array electrode in which anodic titanium oxide (ATO) nanotubes were rooted on a titanium (Ti) current collector as the inert

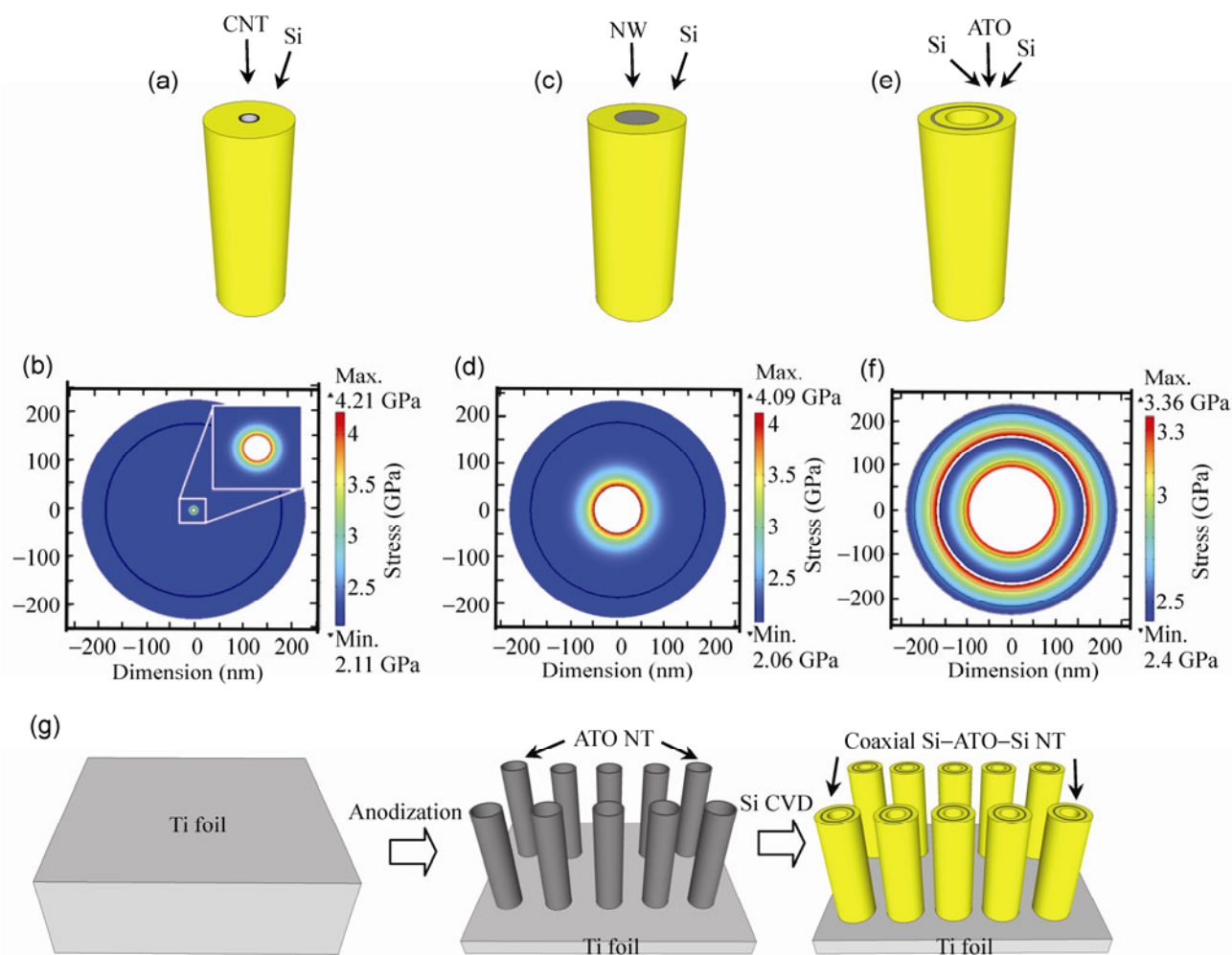


Figure 1 Schematic diagrams (a, c, e) and finite element modeling (b, d, f) of the CNT–Si core–shell structure (a, b), the NW–Si core–shell structure (c, d), and the coaxial Si–ATO–Si nanotube structure (e, f). (g) Schematic representation of the fabrication process for the coaxial Si–ATO–Si nanotube structure.

scaffold in the voltage window 0.01–1 V vs. Li/Li⁺, and the outer and inner Si shell worked as the active material to store Li⁺ (as shown in Fig. 1(g)). This novel coaxial design incorporates all the key features of a high performance lithium-ion battery anode. The ATO scaffold provides a rough surface for improved Si adhesion, and direct contact with the Ti substrate working as current collector. More importantly, Si layers were coated on both outer and inner surfaces of the ATO nanotube array scaffold, leaving abundant space between nanotubes as well as inside each tube, which allowed for better accommodation of volume expansion, both outwards and inwards. We first used theoretical modeling to confirm our hypothesis that the coaxial Si–ATO–Si nanotube has superior mechanical stability compared with some other recently reported Si-based nanostructures. Experimentally fabricating coaxial Si–ATO–Si nanotube array electrodes and measuring the electrochemical performance as a lithium-ion battery anode further validated the feasibility of our proposal. We achieved a high first discharge (lithiation) capacity of 2,824 mAh/g at a current density of 140 mA/g and long-cycling tests achieved stable cycling performance with capacity of over 1,500 mAh/g at 1,400 mA/g current density, which means less than 5% capacity degradation for 100 cycles. Excellent rate capability was also demonstrated.

2 Results and discussion

2.1 Numerical simulation results

Finite element modeling has been recently explored to numerically simulate stress evolution in electrode materials to help better understand the process of high-stress buildup [25]. The high-stress buildup may eventually lead to mechanical fracture and isolation of the electrode material from the metallic current collector, and this is regarded as the key issue in solving the capacity fading problem associated with many electrode materials, such as Si and LiMn₂O₄. Here, we adapted a finite element model developed by Lu [25] to calculate the stress distribution caused by volume change due to Li⁺ intercalation. By comparing the maximum stress existing in our coaxial Si–ATO–Si nanotube array structure with two other recently

reported types of high performance Si-based nanocomposites [26–28], we found the coaxial Si–ATO–Si nanotube array structure we proposed in this paper has the lowest maximum hydrostatic stress indicating it has lowest risk of mechanical fracture and highest stability during charge–discharge cycling. The three nanocomposites we studied were (1) a carbon nanotube (CNT)–Si core–shell structure [26], with 10 nm CNT diameter (Figs. 1(a) and 1(b)), (2) a NW–Si core–shell structure, with 100 nm NW diameter (Figs. 1(c) and 1(d)), where the inner NW can be TiC NW [27] or copper NW [28], and (3) the coaxial Si–ATO–Si nanotube structure, with 300 nm and 340 nm as ATO nanotube inner diameter and outer diameter (Figs. 1(e) and 1(f)). In our models, the loadings of Si was the same per unit length of CNT, NW, and ATO nanotube, which were calculated to give 174 nm and 136 nm thick Si layers on the CNT and NW respectively, and 50 nm layers on both inner and outer surfaces of the ATO nanotube. Considering the uniformity in the longitudinal direction of all three nanocomposites, the calculations were carried out on two-dimensional cross-sections. ATO nanotubes do not participate in lithiation/delithiation after the first cycle between 0.0–1 V and therefore experience no volume change. Thus, in the numerical simulation, ATO nanotubes are fixed in dimension.

The elastic field was taken into consideration when solving the diffusion problem to obtain the concentration and stress profile. The diffusion flux J is given by

$$J = -D(\nabla c - (\Omega c/RT)\nabla \sigma_h) \quad (1)$$

where c is the concentration of lithium ions, D is diffusion coefficient, R is the gas constant, T is the absolute temperature, σ_h is the hydrostatic stress, and Ω is the partial molar volume. The two terms on the right side of Eq. (1) take care of the effect of Li⁺ concentration gradient and stress gradient due to Li⁺ insertion.

Applying the mass conservation equation, $\partial c/\partial t + \nabla \cdot J = 0$, we can obtain the hydrostatic stress σ_h by satisfying the equality,

$$\partial c/\partial t - \nabla \cdot (D(\nabla c - (\Omega c/RT)\nabla \sigma_h)) = 0 \quad (2)$$

The hydrostatic stress can be calculated and mapped using FEMLAB (COMSOL Multiphysics) by applying a constant current boundary condition

$$\mathbf{J} \cdot \mathbf{n} = i_n / F \quad (3)$$

where \mathbf{n} is the normal vector of the surface, i_n is the current density, and F is Faraday's constant.

The hydrostatic stress profiles of the three structures in Figs. 1(a), 1(c), and 1(e) are plotted in Figs. 1(b), 1(d), and 1(f), respectively. The maximum hydrostatic stresses existing in (1) the CNT–Si core–shell structure (Fig. 1(b)), (2) the NW–Si core–shell structure (Fig. 1(d)), and (3) the coaxial Si–ATO–Si nanotube structure (Fig. 1(f)) are 4.2, 4.1, and 3.4 GPa, respectively. The corresponding composition is $\text{Li}_{15}\text{Si}_4$ for all structures. The positions of the maximum stress were located at the innermost layer of the Si shell for all three cases. The structures we propose in this paper had lowest maximum hydrostatic stress, indicating they had lowest risk of mechanical fracture and highest stability during charge–discharge cycling. This may result from the difference in Si-layer thickness. The coaxial Si–ATO–Si nanotube structure had the thinnest Si-layer thickness of 50 nm on both inner and outer sides of the ATO tubes, as well as the smallest maximum stress of 3.4 GPa. In comparison, the CNT–Si core–shell structure had the thickest Si-layer thickness of 174 nm and the largest maximum stress of 4.2 GPa. We stress that our ATO scaffolds provide a rather unique advantage in that silicon can be loaded on both inner and outer surfaces, and an inner pore can still be maintained to provide space for silicon volume expansion. Those features cannot be obtained with the CNT or NW scaffold structures.

2.2 Electrode fabrication and characterization

Coaxial Si–ATO–Si nanotube array electrodes were experimentally fabricated by employing a template approach using ATO nanotubes, as shown by the schematic illustration in Fig. 1(g). The ATO scaffold was first prepared by anodization of Ti foil [29], and it provided both mechanical support as well as a charge transport path for the active amorphous Si layer on both inner and outer surfaces. In addition, ATO nanotubes do not react with lithium in the

voltage window 0.01–1 V vs. Li/Li^+ , as confirmed by our cyclic voltammetry (CV) measurements (Fig. 3(a)). We successfully obtained ATO nanotubes with diameters of 100 to 300 nm and lengths of 1 to 10 μm by utilizing different reaction times and voltages. Then, an amorphous Si layer, functioning as the Li storage medium, was conformally coated on the surface of the ATO nanotube scaffold by chemical vapor deposition (CVD). In this way, the mass ratio of the Si layers to the ATO scaffold could be tuned by varying the thickness of Si coating, which could be easily controlled by CVD time. The Si layer needs to be thick enough to provide a reasonable loading and thinner than the fracture threshold to avoid losing structural integrity during lithiation–delithiation cycling. Different Si layer thicknesses ranging from 20 to 80 nm and different ATO nanotube lengths were tested, and no obvious difference in terms of electrochemical performance was observed.

The morphology and composition of the as-synthesized ATO nanotube array was first characterized by scanning electron microscopy (SEM). Figure 2(a) shows that a vertically aligned ATO nanotube array with uniform diameter was obtained. The morphology of the ATO nanotubes was further characterized by transmission electron microscopy (TEM), as shown in Fig. 2(b). The ATO nanotubes have an inner radius (R_{in}) of 150 nm and an outer radius (R_{out}) of 170 nm. The rough external and internal surfaces of the ATO nanotubes, intrinsically resulting from the anodization process, should enhance the adherence of Si, which has been shown to be a key factor governing the electrochemical performance of lithium-ion batteries [19, 30–34]. The elemental distribution in the ATO nanotubes was analyzed by energy dispersive X-ray (EDX) spectroscopy line scan over the cross-section of one nanotube (Fig. 2(c)). The opposite trend of signal intensity between oxygen (O) and Ti over scanning distance is because the O signal is solely from ATO, while the Ti signal is from both ATO and the Ti substrate beneath, which explains why Ti exhibits higher signal intensity over the void space in the center. Coaxial Si–ATO–Si nanotubes were fabricated by Si deposition on ATO nanotubes by CVD. Coaxial Si–ATO–Si nanotube fragments were generated by performing sonication on a coaxial Si–ATO–Si nanotube

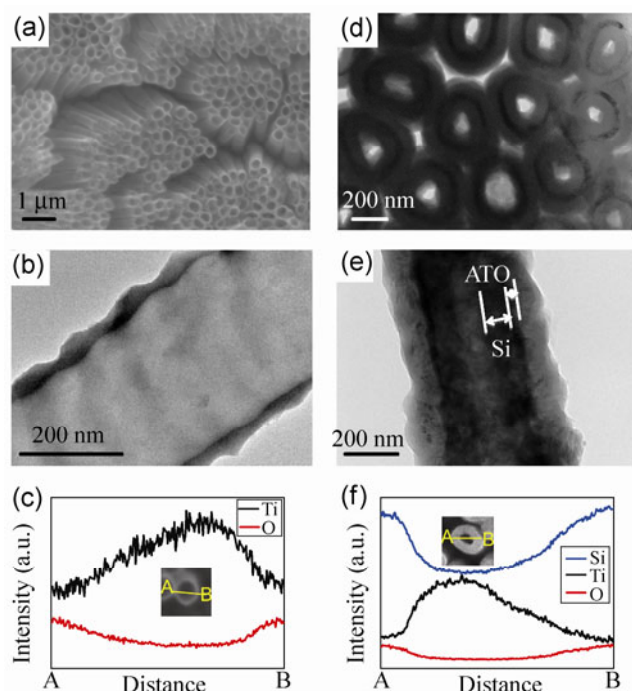


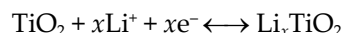
Figure 2 Characterization of ATO and coaxial Si-ATO-Si nanotubes. (a) SEM of as-prepared ATO nanotubes on a Ti substrate. (b) TEM image of an as-prepared ATO nanotube. (c) EDX line scan profile over an ATO nanotube (from point A to point B in Fig. 2(c) inset). (d) TEM image of the cross-section view of a coaxial Si-ATO-Si nanotube. (e) TEM image of the side view of a coaxial Si-ATO-Si nanotube. (f) EDX line scan profile over a coaxial Si-ATO-Si nanotube (from point A to point B in Fig. 2(f) inset).

array and characterized by TEM, as shown in Fig. 2(d). Both cross-section view (Fig. 2(d)) and side view (Fig. 2(e)) revealed a coaxial Si-ATO-Si structure with a uniform 50 nm conformal Si coating on both inner and outer surfaces of the ATO nanotubes. Si distribution was investigated by EDX (Fig. 2(f)), confirming that Si was symmetrically distributed on both inner and outer surfaces of the ATO nanotubes. After coating a 50 nm Si layer on the ATO nanotubes, the outermost few-nanometer thick portion at the surface will be oxidized to SiO_x when exposed to air. Oxygen signals in EDX could be from both the thin layer of SiO_x and the ATO nanotube inside.

2.3 Electrochemical measurements

After fabrication of the coaxial Si-ATO-Si nanotube array on Ti substrate, we evaluated its electrochemical performance. Figure 3(a) shows typical CV curves of the ATO nanotube array scaffold before and after Si

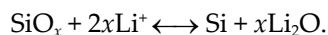
deposition over the voltage window 0.01–1 V vs. Li/Li^+ at a scan rate of 0.1 mV/s. ATO nanotubes with no Si coating exhibited electrochemical double-layer capacitor behavior with no peak related to reaction with lithium, which confirmed the inactive nature of ATO as a scaffold. Although titanium oxide is a widely studied anode material reacting with lithium as



at 1.7 V vs. Li/Li^+ [35], we limited the voltage window between 0.01–1 V vs. Li/Li^+ for both CV and galvanostatic charge–discharge measurements, so TiO_2 did not participate in lithiation/delithiation reactions with lithium and hence ATO just functioned as inert scaffold in this study. After Si deposition, the shape of the CV curve changed dramatically, and signature peaks of Si–Li alloying/dealloying reactions were observed. The peak at 0.19 V in the cathodic branch (lithiation) corresponds to the conversion of amorphous Si to Li_xSi . In the anodic branch (delithiation), the two peaks at 0.35 V and 0.52 V are attributed to the delithiation of Li_xSi back to amorphous Si [36].

Two-electrode 2032 type coin cells were assembled with a coaxial Si-ATO-Si nanotube array grown on Ti current collector as working electrode and lithium metal as the counter electrode to investigate its electrochemical performance. No binder or carbon black additives were employed. A Teklon® polymer separator was used in our coin cells. 1.0 M LiPF_6 in 1:1 w/w ethylene carbonate/diethyl carbonate was used as electrolyte. Figure 3(b) shows the voltage profile for the 1st, 2nd, and 50th cycles of galvanostatic charge–discharge measurement at the same current rate of 140 mAh/g. For the first discharge (lithiation) and charge (delithiation), the specific capacity reached 3,803 mAh/g and 2,802 mAh/g respectively, taking only the Si mass into consideration. The Coulombic efficiency in the first cycle was 73.7% and approached above 95% at all charge–discharge rates after the first cycle. The limited Coulombic efficiency in the first cycle and the improved performance thereafter could result from the formation of a solid electrolyte interphase (SEI) on the electrode surface, which consumes Li^+ in an irreversible manner. In addition, the silicon oxide (SiO_x) formed on the Si surface during

its exposure to air could also contribute to the restricted Coulombic efficiency in the first cycle. The reaction between SiO_x and lithium is partially reversible, and the reversibility depends [28, 37] on the value of x in the equation



Both processes mentioned above mainly occurred in the first cycle and were then suppressed or slowed down, thus resulting in the limited Coulombic efficiency in the first cycle and significant improvement afterwards.

As shown in Fig. 3(c), the coaxial Si-ATO-Si nanotube array electrode exhibited stable cycling

performance at different current rates of 140, 280, 700, and 1,400 mA/g. The discharge capacities at each current rate were 2,717, 2,260, 1,823, and 1,480 mAh/g, respectively. The discharge capacity at 1,400 mA/g, at which rate it took around 1 h to fully discharge or charge the battery, was higher than the theoretical capacity of a graphite electrode by a factor of four. The long-cycling performance of coaxial Si-ATO-Si nanotube array electrodes was also explored by continuous charge and discharge at 1,400 mA/g for 100 cycles after the first cycle (Fig. 3(d)). The discharge capacity for the second and the 101st cycle were 1,624 and 1,548 mAh/g respectively, corresponding to a 4.7% degradation for 100 cycles or less than 0.05%

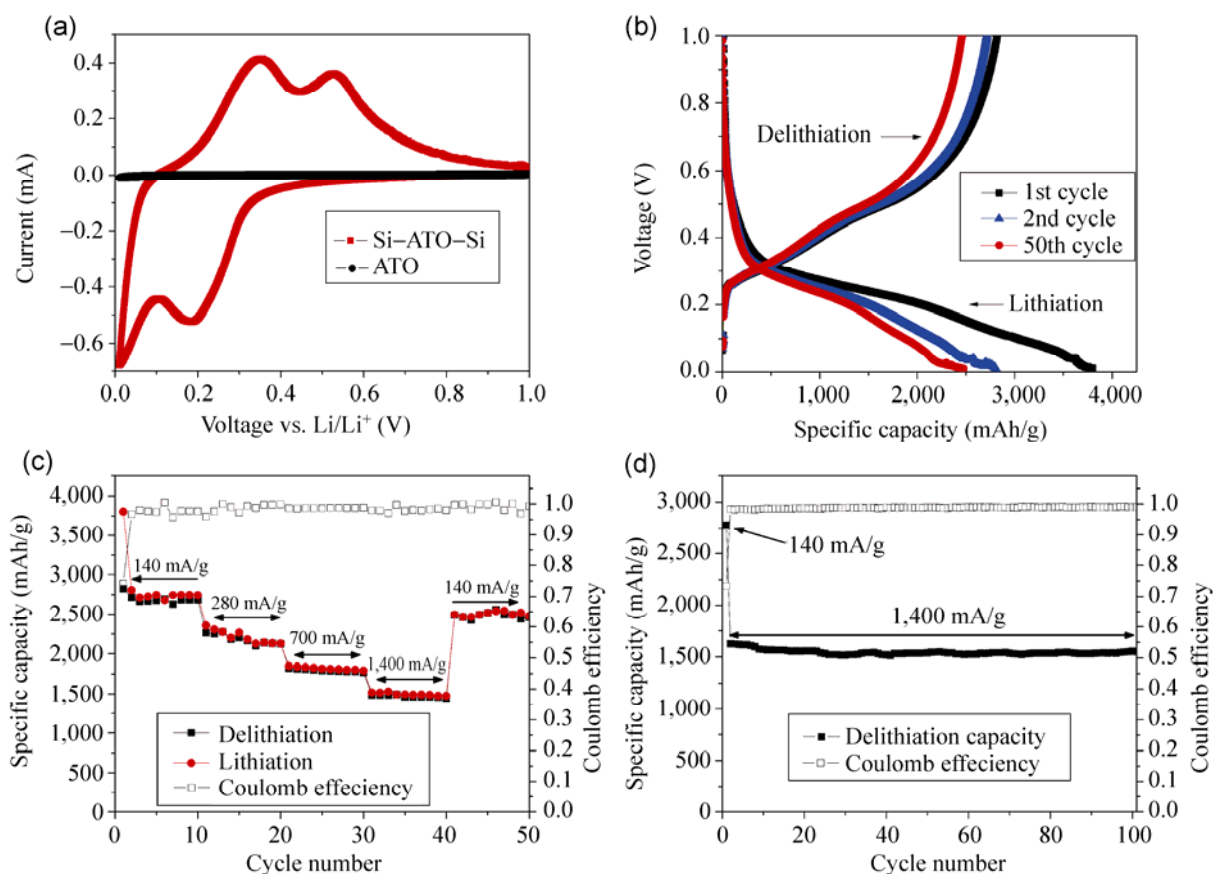


Figure 3 Electrochemical performance of a coaxial Si-ATO-Si nanotube anode. (a) Typical cyclic voltammetry curve comparison of the ATO scaffold and coaxial Si-ATO-Si nanotube, showing the inert nature of ATO with Li^+ between 0.01–1 V vs. Li/Li^+ . (b) Galvanostatic charge-discharge voltage profile between 0.01–1 V vs. Li/Li^+ for the 1st, 2nd, and 50th cycle at 140 mA/g. (c) Plots of charge-discharge specific capacity and Coulombic efficiency vs. cycle number for 50 cycles at different rates ranging from 140 mA/g to 1,400 mA/g. Only the mass of Si is considered for specific capacity calculations. (d) Plots of discharge specific capacity and Coulombic efficiency vs. cycle number at 1,400 mA/g with voltage window between 0.01–1 V vs. Li/Li^+ , under which conditions it takes around 1 h to charge or discharge the battery.

decay per cycle, indicating an excellent cycling stability of the electrode. The retained capacity of 1,548 mAh/g after 100 charge–discharge cycles was still more than four times higher than the theoretical capacity of graphite. Besides the high gravimetric specific capacity achieved, the estimated volumetric specific capacity of around 2,800 mAh/cm³, is also around 3.5 times of that of graphite (800 mAh/cm³) (details of the calculation are given in the Electronic Supplementary Material (ESM)). The electrode also demonstrated favorable Coulombic efficiency, which rapidly recovered to over 98% after the first cycle, and further increased to more than 99% after 10 cycles.

The excellent electrochemical performance of the coaxial Si–ATO–Si nanotube array electrode can be attributed to: (1) the ATO nanotube array providing an excellent inactive, mechanically strong scaffold which survives charge–discharge cycling intact; (2) the ATO nanotube scaffold providing direct contact with the Ti substrate working as current collector, which enhances both the power density and energy density of the lithium-ion battery by minimizing internal resistance and the usage of non-active materials; (3) the rough surface and special geometry of the ATO nanotubes which not only provides an ideal interface for enhanced adhesion between Si and ATO, but also behaves as a superior host for Si with lower stress associated with lithiation; (4) Si being loaded on both the inner and outer surfaces of ATO scaffolds, and an inner pore being maintained to provide room for Si volume expansion. In addition to the justification by simulation and battery performance above, these effects were further confirmed as follows. Batteries with coaxial Si–ATO–Si nanotube array electrodes were disassembled after 10 charge–discharge cycles, and rinsed with acetonitrile and 1 M HCl consecutively to remove residual electrolyte and SEI. The morphology and composition were characterized by SEM and EDX. As expected, the coaxial Si–ATO–Si nanotube array electrode showed limited change in terms of morphology and composition after cycling, which agrees with the stable cycling performance we observed. SEM images (Figs. 4(a) and 4(b)) and EDX line scan profiles of Si, Ti, and O (Fig. 4(c)) confirmed the coaxial Si–ATO–Si nanotube array electrode survived charge–discharge cycling intact.

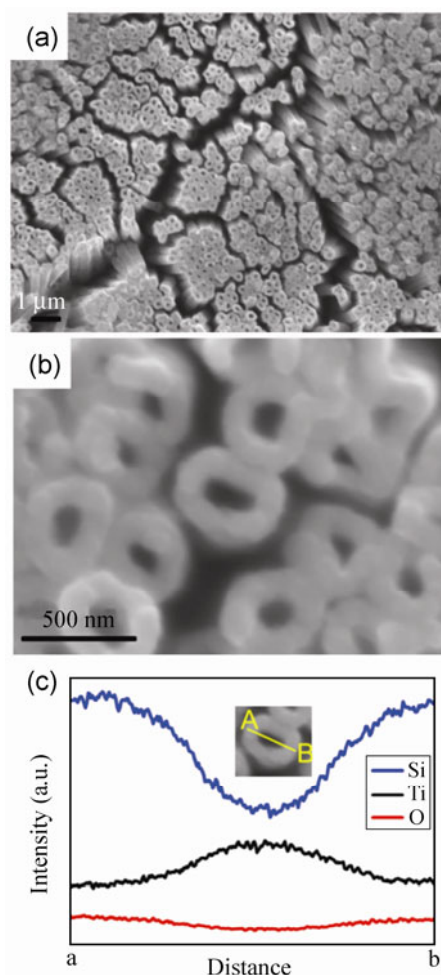


Figure 4 (a, b) SEM images of coaxial Si–ATO–Si nanotubes after 10 charge–discharge cycles and rinsed in acetonitrile and 1 M HCl consecutively to remove residual electrolyte and SEI. (c) EDX line scan profiles of Si (blue), Ti (black), and O (red) over one coaxial Si–ATO–Si nanotube (from point A to point B in Fig. 4(c) inset).

3 Conclusion

We have successfully fabricated coaxial Si–ATO–Si nanotube array structures and employed this novel structure as a lithium-ion battery anode. The coaxial Si–ATO–Si nanotube array demonstrated high specific capacity and excellent cycling performance. After 100 cycles, the capacity still remained above 1,500 mAh/g and the capacity decay was less than 0.05% per cycle. This excellent cycling stability is due to the unique coaxial structure in which ATO provides a strong inert scaffold, a rough surface for Si adhesion, and minimizes the stress upon lithiation of the Si layer by maintaining an inner pore, as was also proven by

simulation. This novel structure is thus a promising candidate for an anode material giving improved lithium-ion battery performance.

4 Experimental

4.1 ATO nanotube array synthesis

The ATO nanotube array was directly formed on a Ti substrate by potentiostatic anodization at 70 V vs. a carbon counter electrode in diethylene glycol electrolyte (DEG) containing 1% HF. The anodization was continuously carried out for 19 h at room temperature. After anodization, the ATO nanotube array on top of the Ti substrate was rinsed with ethanol and naturally dried in air.

4.2 Coaxial Si-ATO-Si nanotube synthesis

An amorphous Si layer, functioning as the Li storage medium, was deposited on an ATO nanotube scaffold by CVD of silane (2% SiH₄ balanced in Ar) at 530 °C for 10 min in a quartz tube furnace (1 inch diameter). The total chamber pressure was 100 Torr. The thickness of the Si coating could be easily controlled by varying the reaction time.

Acknowledgements

We acknowledge the University of Southern California for financial support.

Electronic Supplementary Material: Supplementary material (analysis of first lithiation, parameters used in simulation) is available in the online version of this article at <http://dx.doi.org/10.1007/s12274-013-0294-x>.

References

- [1] Scrosati, B. Battery technology-challenge of portable power. *Nature* **1995**, *373*, 557–558.
- [2] Tarascon, J. M.; Armand, M. Issues and challenges facing rechargeable lithium batteries. *Nature* **2001**, *414*, 359–367.
- [3] Armand, M.; Tarascon, J. M. Building better batteries. *Nature* **2008**, *451*, 652–657.
- [4] Rolison, D. R.; Nazar, L. F. Electrochemical energy storage to power the 21st century. *MRS Bull.* **2011**, *36*, 486–493.
- [5] Goodenough, J. B.; Kim, Y. Challenges for rechargeable Li batteries. *Chem. Mater.* **2010**, *22*, 587–603.
- [6] Liu, J.; Cao, G. Z.; Yang, Z. G.; Wang, D. H.; Dubois, D.; Zhou, X. D.; Graff, G. L.; Pederson, L. R.; Zhang, J. G. Oriented nanostructures for energy conversion and storage. *ChemSusChem* **2008**, *1*, 676–697.
- [7] Oumellal, Y.; Rougier, A.; Nazri, G. A.; Tarascon, J. M.; Aymard, L. Metal hydrides for lithium-ion batteries. *Nat. Mater.* **2008**, *7*, 916–921.
- [8] Bruce, P. G.; Scrosati, B.; Tarascon, J. M. Nanomaterials for rechargeable lithium batteries. *Angew. Chem., Int. Ed.* **2008**, *47*, 2930–2946.
- [9] Sun, Y. K.; Myung, S. T.; Park, B. C.; Prakash, J.; Belharouak, I.; Amine, K. High-energy cathode material for long-life and safe lithium batteries. *Nat. Mater.* **2009**, *8*, 320–324.
- [10] Huang, J. Y.; Zhong, L.; Wang, C. M.; Sullivan, J. P.; Xu, W.; Zhang, L. Q.; Mao, S. X.; Hudak, N. S.; Liu, X. H.; Subramanian, A. et al. *In situ* observation of the electrochemical lithiation of a single SnO₂ nanowire electrode. *Science* **2010**, *330*, 1515–1520.
- [11] Ji, X. L.; Evers, S.; Black, R.; Nazar, L. F. Stabilizing lithium-sulphur cathodes using polysulphide reservoirs. *Nat. Commun.* **2011**, *2*, 325.
- [12] Zhang, H. G.; Yu, X. D.; Braun, P. V. Three-dimensional bicontinuous ultrafast-charge and -discharge bulk battery electrodes. *Nat. Nanotechnol.* **2011**, *6*, 277–281.
- [13] Malik, R.; Zhou, F.; Ceder, G. Kinetics of non-equilibrium lithium incorporation in LiFePO₄. *Nat. Mater.* **2011**, *10*, 587–590.
- [14] Boukamp, B. A.; Lesh, G. C.; Huggins, R. A. All-solid lithium electrodes with mixed-conductor matrix. *J. Electrochem. Soc.* **1981**, *128*, 725–729.
- [15] Chan, C. K.; Peng, H. L.; Liu, G.; Mcilwrath, K.; Zhang, X. F.; Huggins, R. A.; Cui, Y. High-performance lithium battery anodes using silicon nanowires. *Nat. Nanotechnol.* **2008**, *3*, 31–35.
- [16] Cui, L. F.; Ruffo, R.; Chan, C. K.; Peng, H. L.; Cui, Y. Crystalline-amorphous core-shell silicon nanowire for high capacity and high current battery electrodes. *Nano Lett.* **2009**, *9*, 491–495.
- [17] Chen, H. T.; Xu, J.; Chen, P. C.; Fang, X.; Qiu, J.; Fu, Y.; Zhou, C. W. Bulk synthesis of crystalline and crystalline core/amorphous shell silicon nanowires and their application for energy storage. *ACS Nano* **2011**, *5*, 8383–8390.
- [18] Cui, L. F.; Yang, Y.; Hsu, C. M.; Cui, Y. Carbon-silicon core-shell nanowires as high capacity electrodes for lithium ion batteries. *Nano Lett.* **2009**, *9*, 3370–3374.
- [19] Magasinski, A.; Dixon, P.; Hertzberg, B.; Kvit, A.; Ayala, J.; Yushin, G. High-performance lithium-ion anode using a hierarchical bottom-up approach. *Nat. Mater.* **2010**, *9*, 353–358.

- [20] Rong, J. P.; Masarapu, C.; Ni, J.; Zhang, Z. J.; Wei, B. Q. Tandem structure of porous silicon film on single-walled carbon nanotube macrofilms for lithium-ion battery applications. *ACS Nano* **2010**, *4*, 4683–4690.
- [21] Zhou, S.; Liu, X. H.; Wang, D. W. Si/TiSi₂ heteronanostructures as high-capacity anode material for Li ion batteries. *Nano Lett.* **2010**, *10*, 860–863.
- [22] Kim, H.; Han, B.; Choo, J.; Cho, J. Three-dimensional porous silicon particles for use in high-performance lithium secondary batteries. *Angew. Chem., Int. Ed.* **2008**, *47*, 10151–10154.
- [23] Yao, Y.; McDowell, M. T.; Ryu, I.; Wu, H.; Liu, N.; Hu, L. B.; Nix, W. D.; Cui, Y. Interconnected silicon hollow nanospheres for lithium-ion battery anodes with long cycle life. *Nano Lett.* **2011**, *11*, 2949–2954.
- [24] Song, T.; Xia, J. L.; Lee, J. H.; Lee, D. H.; Kwon, M. S.; Choi, J. M.; Wu, J.; Doo, S. K.; Chang, H.; Park, W. II. et al. Arrays of sealed silicon nanotubes as anodes for lithium ion batteries. *Nano Lett.* **2010**, *10*, 1710–1716.
- [25] Park, J.; Lu, W.; Sastry, A. M. Numerical simulation of stress evolution in lithium manganese dioxide particles due to coupled phase transition and intercalation. *J. Electrochem. Soc.* **2011**, *158*, A201–A206.
- [26] Evanoff, K.; Khan, J.; Balandin, A. A.; Magasinski, A.; Ready, W. J.; Fuller, T. F.; Yushin, G. Towards ultrathick battery electrodes: Aligned carbon nanotube – enabled architecture. *Adv. Mater.* **2012**, *24*, 533–537.
- [27] Yao, Y.; Huo, K. F.; Hu, L. B.; Liu, N.; Cha, J. J.; McDowell, M. T.; Chu, P. K.; Cui, Y. Highly conductive, mechanically robust, and electrochemically inactive TiC/C nanofiber scaffold for high-performance silicon anode batteries. *ACS Nano* **2011**, *5*, 8346–8351.
- [28] Cao, F. F.; Deng, J. W.; Xin, S.; Ji, H. X.; Schmidt, O. G.; Wan, L. J.; Guo, Y. G. Cu–Si nanocable arrays as high-rate anode materials for lithium-ion batteries. *Adv. Mater.* **2011**, *23*, 4415–4420.
- [29] Yoriya, S.; Grimes, C. A. Self-assembled TiO₂ nanotube arrays by anodization of titanium in diethylene glycol: Approach to extended pore widening. *Langmuir* **2010**, *26*, 417–420.
- [30] Beaulieu, L. Y.; Eberman, K. W.; Turner, R. L.; Krause, L. J.; Dahn, J. R. Colossal reversible volume changes in lithium alloys. *Electrochem. Solid-State Lett.* **2001**, *4*, A137–A140.
- [31] Park, M. S.; Wang, G. X.; Liu, H. K.; Dou, S. X. Electrochemical properties of Si thin film prepared by pulsed laser deposition for lithium ion micro-batteries. *Electrochim. Acta* **2006**, *51*, 5246–5249.
- [32] Moon, T.; Kim, C.; Park, B. Electrochemical performance of amorphous-silicon thin films for lithium rechargeable batteries. *J. Power Sources* **2006**, *155*, 391–394.
- [33] Yin, J. T.; Wada, M.; Yamamoto, K.; Kitano, Y.; Tanase, S.; Sakai, T. Micrometer-scale amorphous Si thin-film electrodes fabricated by electron-beam deposition for Li-ion batteries. *J. Electrochem. Soc.* **2006**, *153*, A472–A477.
- [34] Kim, Y. L.; Sun, Y. K.; Lee, S. M. Enhanced electrochemical performance of silicon-based anode material by using current collector with modified surface morphology. *Electrochim. Acta* **2008**, *53*, 4500–4504.
- [35] Yang, Z. G.; Choi, D.; Kerisit, S.; Rosso, K. M.; Wang, D. H.; Zhang, J.; Graff, G.; Liu, J. Nanostructures and lithium electrochemical reactivity of lithium titanates and titanium oxides: A review. *J. Power Sources* **2009**, *192*, 588–598.
- [36] Li, J.; Dahn, J. R. An *in situ* X-ray diffraction study of the reaction of Li with crystalline Si. *J. Electrochem. Soc.* **2007**, *154*, A156–A161.
- [37] Chen, X. L.; Gerasopoulos, K.; Guo, J. C.; Brown, A.; Wang, C. S.; Ghodssi, R.; Culver, J. N. Virus-enabled silicon anode for lithium-ion batteries. *ACS Nano* **2010**, *4*, 5366–5372.